

## High-contrast L-band Integral Field Spectroscopy of HD 33632 Ab

JORDAN M. STONE <sup>1</sup>, STEVE ERTTEL <sup>2,3</sup>, TRAVIS BARMAN <sup>4</sup>, ANDREW J. I. SKEMER <sup>5</sup>, JARRON M. LEISENRING <sup>6</sup>, PHILIP M. HINZ <sup>5</sup>,  
CHARLES E. WOODWARD <sup>7</sup> AND MICHAEL F. SKRUTSKIE<sup>8</sup>

<sup>1</sup>Naval Research Laboratory, Remote Sensing Division, 4555 Overlook Ave SW, Washington, DC 20375 USA

<sup>2</sup>Department of Astronomy and Steward Observatory, University of Arizona, 933 N. Cherry Ave, Tucson, AZ 85721-0065 USA

<sup>3</sup>Large Binocular Telescope Observatory, University of Arizona, 933 N. Cherry Ave, Tucson, AZ 85721-0065 USA

<sup>4</sup>Lunar and Planetary Laboratory, The University of Arizona, 1629 E. Univ. Blvd., Tucson, AZ 85721 USA

<sup>5</sup>Department of Astronomy and Astrophysics, University of California, Santa Cruz, 1156 High St, Santa Cruz, CA 95064, USA

<sup>6</sup>Steward Observatory, University of Arizona, 933 N. Cherry Ave, Tucson, AZ 85721-0065 USA

<sup>7</sup>Minnesota Institute for Astrophysics, School of Physics and Astronomy, 116 Church Street, S.E., University of Minnesota, Minneapolis, MN 55455, USA

<sup>8</sup>Department of Astronomy, University of Virginia, Charlottesville, VA 22904, USA

### ABSTRACT

We present LBTI/ALES 3.07 – 4.08 $\mu$ m spectroscopic observations of HD 33632 Ab, a  $\sim 53 M_{Jup}$  directly imaged companion to an F8 star. Spectroscopic measurements of HD 33632 Ab now span 1 – 4  $\mu$ m, and we perform the first spectroscopic analysis covering this full range. The data are compared to isolated brown dwarf template spectra, indicating that HD 33632 Ab is similar to L8/9 field brown dwarfs. Synthetic atmosphere model spectra from multiple model families are fit, with cloudy models providing the best fits, consistent with expectations for an L-dwarf. Evolutionary model predictions for the bulk properties of HD 33632 Ab are highly constrained by the precise dynamical mass found for the object. In particular, predictions for surface gravity are narrowly peaked,  $\log(g) = 5.21 \pm 0.05$ , and not dependent on the effects of clouds or cloud dispersion. We find significant tension between the surface gravities and object radii inferred from atmosphere model fits and those predicted by evolutionary models. We conclude with a comparison to the spectra of the HR 8799 c, d, and e, and emphasize the case that HD 33632 Ab, and other L/T transition directly imaged companions with constrained masses, will serve an essential role in understanding the complex physical processes governing the appearance of clouds in planetary atmospheres.

*Keywords:* Extrasolar gas giants, Instrumentation

### 1. INTRODUCTION

The *Gaia* mission (Gaia Collaboration et al. 2016) is transforming the way exoplanet direct imaging science is done. The most obvious impact is the increased efficiency of direct imaging searches, with several newly discovered high-contrast substellar companions arising from target lists composed of stars showing astrometric acceleration (e.g., HD 33632 Ab, HIP 21152 B, HD 99770 b, AF Lep b, HIP 39017 b T. Currie et al. 2020; M. Bonavita et al. 2022; T. Currie et al. 2023; D. Mesa et al. 2023; T. L. Tobin et al. 2024). Recent results show substellar companion detection rates as high as 16% when using *Gaia*-assisted targeted searches compared to  $\lesssim 1\%$  for blind searches (M. Bonavita et al. 2022; J. M. Stone et al. 2018).

Beyond detection, *Gaia*-assisted direct imaging discoveries are poised for detailed atmospheric characterization because dynamical mass constraints can be harnessed to guide atmosphere modeling, a fact long appreciated by the transiting planet community. Z. Zhang et al. (2023) demonstrated the power of this approach, confidently showing that the directly imaged planet AF Lep b is metal enriched compared to its host star. It is now clear that constraining the fundamental parameters of substellar objects is essential for enabling the most detailed atmospheric characterization and for achieving the goals of the exoplanet community to understand cloud physics, atmospheric dynamics, atmospheric composition, planet formation and evolution (see E. Calamari et al. 2024).

Here we present new spectroscopic measurements of HD 33632 Ab, a brown dwarf companion discovered  $\approx 0''.75$  in projected separation from its host star by T. Currie et al. (2020) in a campaign to target astrometric accelerators. M. El Morsy et al. (2025) combine astrometric acceleration measurements with radial velocity and projected separation mea-

measurements to constrain the system orbit and derive a secondary mass of  $52.8^{+2.6}_{-2.4} M_{\text{Jup}}$ .

The host star, HD 33632 Aa, is an F8V type star at 26.38 pc with an estimated age of  $1.5^{+3.0}_{-0.7}$  Gyr (R. O. Gray et al. 2003; Gaia Collaboration et al. 2021; T. Currie et al. 2020). M. Rice & J. M. Brewer (2020) analyze Keck/HIRES observations of HD 33632 Aa and constrain stellar effective temperature, surface gravity and the abundance of several elemental species.

Multiple studies have analyzed infrared spectroscopic measurements of HD 33632 Ab to infer its atmospheric properties. T. Currie et al. (2020) compare near-infrared (NIR) low resolution,  $R \sim 20$ , Subaru/Charis observations covering the J-, H-, and K-bands to brown dwarf spectral templates, finding a best fit of L9.5. Follow-up observations targeting the H- and K-bands at higher spectral resolution with Subaru/Charis are reported by A. B. Gibbs et al. (2024) and M. El Morsy et al. (2025). M. El Morsy et al. (2025) combine these data with L-band photometry from T. Currie et al. (2020) to perform atmosphere model fits, finding best-fit models consistent with evolutionary model predictions. C.-C. Hsu et al. (2024) use the Keck/KPIC module to direct light from HD 33632 Ab into the NIRSPEC instrument for  $R \sim 35000$  spectroscopy within the K-band. These data are harnessed to constrain the rotation velocity of the brown dwarf and to measure chemical abundances, which include a non-detection of methane. Each of the previous studies has made use of a combination of the several spectral ranges covered, including JHK, HKL, only H-band or only K-band. Many previous studies demonstrate that using broad wavelength coverage breaks degeneracies in spectroscopic analysis investigating the atmospheres of brown dwarfs (see D. C. Stephens et al. 2009; S. Sorahana & I. Yamamura 2014) and directly imaged companions (see A. J. Skemer et al. 2016; J. M. Stone et al. 2020; D. S. Doelman et al. 2022). The L-band, covering  $\sim 2.9 - 4.1 \mu\text{m}$ , is particularly sensitive to the effects of clouds and non equilibrium carbon chemistry. Here we present the first analysis of spectroscopic measurements spanning J-, H-, K-, and L-band.

## 2. OBSERVATIONS AND DATA REDUCTION

We observed HD 33632 Ab on UT 2021 Feb 28 using the Large Binocular Telescope (LBT). Our setup directed light from the SX (or left side) 8.4 m LBT aperture to the Arizona Lenslets for Exoplanet Spectroscopy (ALES) integral field spectrograph (IFS, A. J. Skemer et al. 2018) mode of the L- and M-band Infrared Camera (LMIRCam) instrument (J. M. Leisenring et al. 2012), which operates within the framework of the Large Binocular Telescope Interferometer (LBTI, P. M. Hinz et al. 2016; S. Ertel et al. 2020). ALES provides  $R \sim 40$  spectra from 2.9 to  $4.2 \mu\text{m}$  over a  $\sim 2''2$  field of view. Our observational setup made use of an 8x refrac-

tive magnifier and a lenslet array with  $500 \mu\text{m}$  lenses, yielding 34.5 milliarcseconds spatial sampling (J. M. Stone et al. 2022). No coronagraph or apodizing optics are used. Light from the DX (or right side) 8.4 m LBT aperture was directed into the PEPSI instrument (K. G. Strassmeier et al. 2015) to enable detailed spectral analysis of the host star, including inference of the system bulk composition. Those data will be reported in a future article.

Observations began just after HD 33632 A transited the meridian. We tracked the system for a total of 140 minutes accumulating  $39^\circ$  of parallactic angle rotation. Atmospheric seeing at visible wavelengths varied from  $1''.1$  to  $1''.5$ . The adaptive optics system was run correcting 400 modes at 1.4 kHz loop speed.

A nodding sequence was used to track variable background emission, collecting 300 1.48s frames on-source and then 300 1.48s frames off source each cycle for a total of 5 cycles, totaling of 33.9 m of on-source exposure time.

### 2.1. Raw Frame Preprocessing

Our 1.48s integrations include three non-destructive reads each. To remove detector reset noise and bias drifts we subtract the first read from the last read of each ramp (the central read is disregarded in our analysis).

We subtract an estimate of the background emission from each on-source frame. To do this, we identify the 200 closest-in-time off-source frames and median combine them. After background subtraction, residual channel offsets are removed using the median of the overscan pixels in the lowest four rows of each channel. Vertical overscan columns are median combined and smoothed with a Savitsky-Golay filter using a 31-pixel window length and a polynomial order of three (W. H. Press & S. A. Teukolsky 1990). The result is subtracted from each column.

Bad pixels are identified using a set of dark frames, modeling the distribution of pixel values as a Gaussian, and finding those pixels with values having less than 1% probability of arising by chance given the more than 4 million pixels in the array. We take the resulting bad pixel mask and correct each bad pixel in our background and overscan corrected images by replacing them with the median of their four closest neighbors.

### 2.2. Creating Spectral Cubes

We transform our two-dimensional images, composed of a grid of short interleaved spectral traces, into data cubes with two spatial dimensions and one wavelength calibrated spectral dimension following the approach described in J. M. Stone et al. (2018), and J. M. Stone et al. (2022). The ALES pipeline uses the optimal extraction algorithm (K. Horne 1986) on each microspectrum sequentially, which can be more susceptible to microspectra cross talk than  $\chi^2$  extrac-

tion technique used in the Charis pipeline (T. D. Brandt et al. 2017).

In order to reduce computer processing time in subsequent analysis steps, we bin our data cubes in the spectral dimension to reduce oversampling. We assume a constant spectral resolution across the band of  $R \sim 40$  (J. M. Stone et al. 2022) and resample the spectrum at each spatial location using the SpectRes package (A. Carnall 2021) to yield three evenly spaced samples per resolution element.

### 2.3. High Contrast Image Processing

The orientation of our images rotates with the parallactic angle, decreasing from  $134^\circ$  to  $85^\circ$  over the course of our observation. We use angular differential imaging (ADI, C. Marois et al. 2006) to process our frames implementing a principal component analysis (PCA, A. Amara & S. P. Quanz 2012; R. Soummer et al. 2012) approach. We treat each wavelength slice individually focusing on an annulus centered on the host star with radius equal to the companion separation and width  $\sim 5\lambda/D$  (12 pixels). For each frame we create a point spread function (PSF) library using all other frames excluding those with the companion position within 2 pixels. After host-star PSF subtraction at each wavelength, images are rotated to orient North up and median combined to produce a final reduced image cube. We tested reductions using 3, 10, and 30 principal components when subtracting the host star; using 3 principal components provided the best signal-to-noise ratio of the companion in the final stacked image. Figure 1 shows the image that results from summing over the wavelength dimension of our final data cube. It is noteworthy that 3 principal components optimizes the reduction given a library of 1500 frames. This results from low illumination of the speckle halo (compared to the thermal background) at the separation of HD 33632 Ab in the ALES data. As we note below, background dominated noise also affects the shape of the spectral covariance matrix.

The signal to noise ratio for HD 33632 Ab is estimated in each wavelength slice using a PSF-weighted mean of pixels within an aperture of radius corresponding to  $\lambda/D$ . Specifically, we take signal as the flux in an aperture centered on the brightest pixel in the wavelength collapsed cube, and noise is estimated as the standard deviation of PSF-weighted flux measurements in non-overlapping apertures in a ring about the primary star with the same projected separation, avoiding regions of significant detector crosstalk (see D. S. Doelman et al. 2022). Signal-to-noise maps created using the same approach are presented in the appendix.

### 2.4. Spectral Extraction

High-contrast image processing algorithms can bias companion photometry due to over subtraction. To accurately extract the flux of HD 33632 Ab we use a forward modeling approach, subtracting a model of the companion from

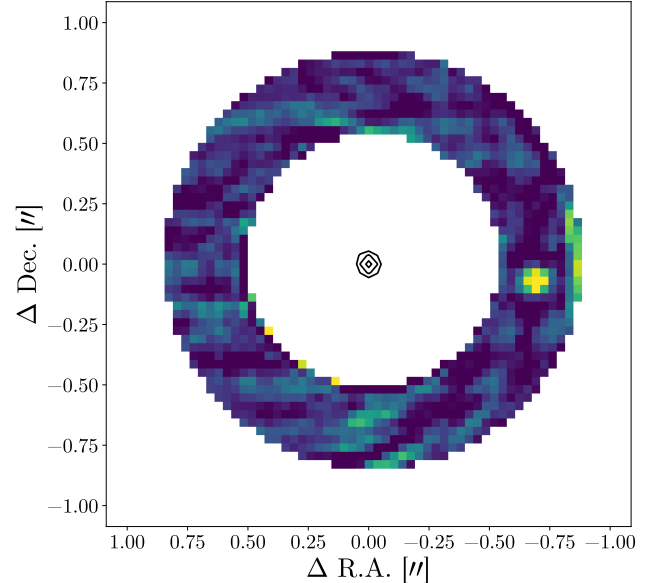


**Figure 1.** The wavelength stacked image of HD 33632 Ab taken with LMIRCam+ALES. The annular region shows the pixels processed with our PCA-based ADI routine. White regions have been masked for display. Black contours near the origin indicate the position of the unsaturated host star.

each frame prior to running PCA PSF optimization. The host star did not saturate in any of our frames, so we use it as a time-resolved PSF reference to model the companion. This provides photometric measurements robust to variable atmospheric throughput and changes in the PSF shape due to instrumental flexure and variable AO-performance. We fit for a scale factor and position of the companion, using the sum of squared residuals ( $\chi^2$ ) in a  $3 \times 3$  pixel region centered on the object as the figure of merit.

Brute force forward modeling is computationally expensive with 1500 frames. Therefore, we choose to ignore 19 wavelength slices between  $3.07 \mu\text{m}$  and  $3.5 \mu\text{m}$  where signal-to-noise as determined using aperture photometry was below 2. For slices with signal-to-noise  $> 2$ , we use a grid-fitting approach to determine the relative brightness of the companion compared to its host star. First, we calculate  $\chi^2$  for 10 scale factors logarithmically spaced between  $10^{-4}$  and  $10^{-3}$  with the companion position fixed at the location of the brightest pixel in the median image. Next, we fit a parabola to the  $\chi^2$  versus scale factor data and identify the scale factor that minimizes the parabola. This scale factor provides a good-guess starting place for our simultaneous fit of position offset and scale factor, described next.

For each of 9 positions on a square grid with quarter-pixel steps, the best-fit scale factor is determined by minimizing a parabola fitted to seven scale factor versus  $\chi^2$  points, four logarithmically spaced between  $\frac{1}{3}$  and 3 times the good guess

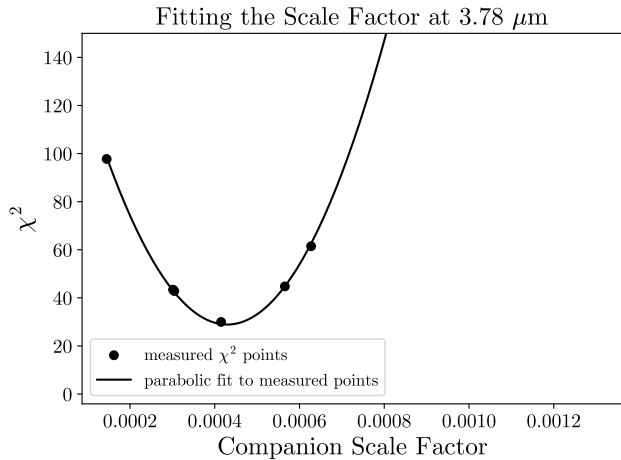


**Figure 2.** Scale factors quantifying the flux ratio between the companion and host star are determined for each wavelength by minimizing a parabola fit to the results of a grid-fitting algorithm.

scale factor and three logarithmically spaced between 0.7 and 1.3 times good guess scale factor. Figure 2 illustrates our approach for the  $3.78 \mu\text{m}$  slice. Minimum  $\chi^2$  values for each wavelength are found with a position offset one quarter pixel to the south of the brightest pixel in the collapsed cube.

We perform flux calibration by multiplying our scale factors by a model spectrum for the host star, smoothed to  $R=40$  and sampled and binned in the same way as our ALES spectral cubes. We use a BT-Settl (I. Baraffe et al. 2015) model with  $T_{\text{eff}} = 6100 \text{ K}$ ,  $\log(g) = 4.5$  (M. Rice & J. M. Brewer 2020), scaled to provide a best fit to WISE W1, W2, W3, and W4 photometry (R. M. Cutri & et al. 2012). Our flux uncertainty is derived using our signal-to-noise measurements described above. Figure 3 presents our final flux calibrated spectrum and uncertainties and compares our results to the Keck/NIRC2 photometric point reported by M. El Morsy et al. (2025). The spectral flux calibration is consistent with the earlier photometry. We tabulate the calibrated spectrum Table 1.

Figure 3 also shows a normalized spectrum of HD 33632 A calculated using aperture photometry using a 3-pixel diameter aperture centered on the brightest pixel seen when the wavelength dimension is median combined. This spectrum is uncalibrated and its shape should include the intrinsic shape of the stellar spectrum (nearly Rayleigh-Jeans at these wavelengths) as well as features arising from chromatic system throughput, including telluric absorption. The most dramatic feature is a strong telluric water-ice absorption band near  $3.2 \mu\text{m}$ . However, this band does not span the full  $3.07 \mu\text{m} - 3.5 \mu\text{m}$  range of wavelengths where the companion is not detected above a signal-to-noise ratio of 2. Evidently, low throughput cannot completely explain our lack of

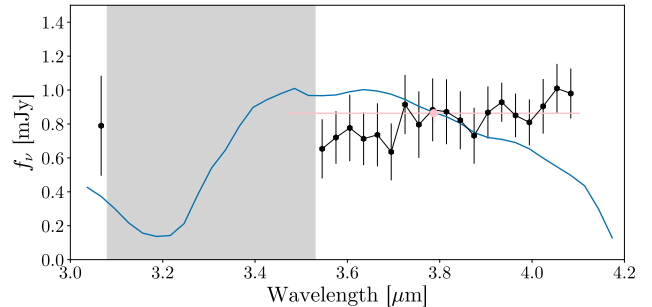


**Figure 3.** The flux calibrated ALES spectrum and uncertainties of HD 33632 Ab (black markers) compared to the T. Currie et al. (2020) Keck/NIRC2 L-band photometric measurement, shown with a pink marker with horizontal errorbars indicating the filter bandwidth and vertical errorbars indicating photometric uncertainty. We indicate with a gray swath a region in which we did not recover the companion with signal-to-noise ratio greater than 2. The blue curve is a normalized, uncalibrated spectrum of the central star, highlighting strong telluric absorption near  $3.2 \mu\text{m}$ .

detections in this band, suggesting low intrinsic flux from the companion at these wavelengths.

Spectral covariance in the calibrated spectrum is estimated using the approach suggested by J. P. Greco & T. D. Brandt (2016). Adhering to the notation of that work, our best-fit model covariance matrix has  $A_\rho = 0.067$ ,  $\sigma_\rho = 10125$ ,  $A_\lambda = 0.37$ ,  $\sigma_\lambda = 0.039$ , and  $A_\delta = 0.56$ . The large value of  $\sigma_\rho$  results from residuals being background dominated, rather than speckle dominated, at the separation of HD 33632 Ab.

### 3. SPECTRAL ANALYSIS

#### 3.1. Compiling low-resolution data

For our spectroscopic analysis, we combine the low spectral resolution integral field spectrograph observations of HD 33632 Ab, forming an  $R \sim 20 - 65$  spectrum spanning  $1.16 - 4.1 \mu\text{m}$  with gaps in regions of strong telluric absorption. For the J-, H-, and K-bands we use published Subaru/Charis data, preferring the available higher-resolution ( $R \sim 65$ ) mode observations for the H-, and K-bands (T. Currie et al. 2020; M. El Morsy et al. 2025). For the combined Charis+ALES data we create a block diagonal covariance matrix taking the J-band errors to be diagonal (T. Currie et al. 2020) and using the published H-, and K-band covariance matrices (M. El Morsy et al. 2025) together with the L-band covariance matrix from the current work.

#### 3.2. Fits to Brown Dwarf Template Spectra

We fit the combined Charis+ALES spectrum of HD 33632 Ab to a library of brown dwarf spectra. The template library is composed of IRTF/Spex and Subaru/IRCS observations of brown dwarfs. Objects are selected for having measurements spanning  $\sim 1 - 4.12 \mu\text{m}$  reported in M. C. Cushing et al. (2005) and/or J. T. Rayner et al. (2009). We

**Table 1.** ALES Spectrum of HD 33632 Ab

$\lambda$	$F_\nu$	$\delta F_\nu$
$\mu\text{m}$	mJy	mJy
3.067	0.790	0.295
3.545	0.653	0.174
3.575	0.720	0.155
3.605	0.777	0.196
3.635	0.713	0.155
3.665	0.736	0.186
3.695	0.635	0.168
3.725	0.915	0.175
3.755	0.796	0.196
3.785	0.883	0.185
3.815	0.872	0.191
3.845	0.822	0.171
3.874	0.731	0.165
3.904	0.868	0.154
3.934	0.928	0.115
3.964	0.851	0.129
3.994	0.810	0.135
4.024	0.904	0.161
4.054	1.010	0.145
4.084	0.980	0.147

also include the JWST NIRSpec measurements of VHS J1256-1257B from [B. E. Miles & et al. \(2023\)](#). Library objects are summarized in [Table 2](#).

To prepare for fitting, template spectra are smoothed and interpolated to match Charis and ALES spectral resolution and wavelength sampling. Since the errorbars associated with the Charis and ALES high-contrast data are much larger than the Spex, IRCS, and NIRSpec data, we do not propagate template uncertainties.

We perform a  $\chi^2$  minimization to determine the library spectrum that most closely resembles the observations of HD 33632 Ab, using

$$\chi^2(\tau, f) = \left( (fx(\tau) - \mu)^T \Sigma^{-1} (fx(\tau) - \mu) \right), \quad (1)$$

where  $x(\tau)$  represents the template spectrum for the object with spectral type  $\tau$ ,  $f$  is a scale factor,  $\mu$  is the observed spectrum of HD 33632 Ab and  $\Sigma$  is the block-diagonal covariance matrix for the IFS data. For each object we varied  $f$  to find the optimal fit at each spectral type. The results of our fit are presented in [Table 2](#).

The best fit template spectrum is DENIS-P J025503.3-470049, with spectral type  $\sim$ L8/9 ([M. C. Cushing et al. 2005](#); [A. J. Burgasser et al. 2006](#)). We show the template spectrum over plotted on the spectral energy distribution (SED) of HD 33632 Ab in [Figure 4](#). The template provides a quali-

tatively good fit to HD 33632 Ab, especially the J-L, and J-H color. In [Figure 4](#) we also show the second-best template (the L7.5-type) and the spectrum of the low-gravity object VHS 1256-1257 B (L7 $\pm$ 1.5). VHS 1256-1257 B is a poor match to the HD 33632 Ab spectrum, low-gravity resulting in a redder slope than seen for our target.

Fit quality can be evaluated with the reduced  $\chi^2$  metric. Using 56 degrees of freedom the best fit template has  $\chi_r^2 = 3.9$ , suggesting an imperfect but reasonable match. We also evaluate the quality of the fit by comparing the derived scale factor to the expected scale factor. Assuming the template and HD 33632 Ab have the same effective temperature and radius, the scale factor should be the ratio of the distances squared. In [Table 2](#) we show the expected and recovered scale factors for each object and report the difference in units of the uncertainty found by propagating the reported parallax errors. In [Table 2](#) objects with the least tension are those with the largest parallax uncertainty, suggesting insufficient precision to constrain the scale factor in these cases. For other objects, significant tension with the expected scale factor suggests either that the radii are dissimilar and/or that the effective temperature is dissimilar. Among the objects with parallax measured with better than 0.5 milliarcsecond precision, DENIS-P J025503.3-470049 has the least tension with expectations. Systematic issues relating to absolute calibration of the spectra arising from 3 different instruments may explain the residual discrepancy with expectation.

### 3.3. Fitting Synthetic Atmosphere Models

We compare the low-resolution  $\sim 1 - 4.12 \mu\text{m}$  spectrum of HD 33632 Ab to synthetic spectra from four grids of model atmospheres. These grids include three with clouds and one cloud free. The cloudy grids we use are Exo-REM, which includes a microphysics-based cloud exposing no adjustable cloud parameters for model fitting ([J. L. Baudino et al. 2015](#); [B. Charnay et al. 2018](#); [D. Blain et al. 2021](#)), Sonora Diamondback, which includes a single parameter modifying cloud structure (fsed, [C. V. Morley et al. 2024](#)), and the Barman/Brock models, which provide two parameters to adjust the effects of clouds ( $P_c, a_0$ , [T. S. Barman et al. 2011, 2015](#); [L. Brock et al. 2021](#)). The cloud free model grid we use is Sonora Elf Owl, which includes parameters for adjusting both composition and vertical mixing (nonequilibrium chemistry, [S. Mukherjee et al. 2024](#)). Model grid parameter ranges are summarized in [Table 3](#).

Models are smoothed and sampled to match the different IFS instrument modes. We interpolate the Barman/Brock grid to 20 K temperature sampling, and 0.1 dex surface gravity sampling using the same procedure as in [J. M. Stone et al. \(2020\)](#). We chose not to interpolate either Sonora grid. For Diamondback, many of the models are poorly converged ([C. V. Morley et al. 2024](#)) and we opt to avoid interpolating

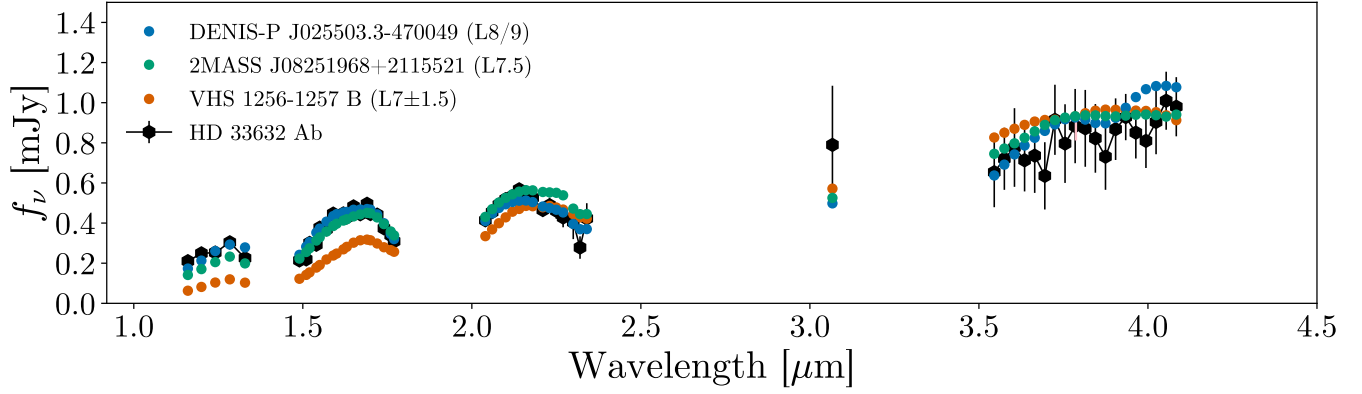


**Figure 4.** Template brown dwarf spectra compared to HD 33632 Ab.

**Table 2.** Brown Dwarf Template Library

Obj. Name	Spectral Type <sup>a</sup>	$\chi^2$	parallax <sup>b</sup>	$f^c$	expected sf. <sup>d</sup>	$N\sigma^e$
GJ 1111	M6.5	431	$279.25 \pm 0.06$	0.0004	0.018	702.815
GJ 644 C	M7	406	$153.97 \pm 0.06$	0.0019	0.061	615.836
LP 412-31	M8	331	$68.27 \pm 0.08$	0.0107	0.308	361.683
DENIS J104814.6-395606	M9V	360	$247.22 \pm 0.05$	0.0015	0.024	648.897
BRI B0021-0214	M9.5	234	$80.34 \pm 0.19$	0.0112	0.222	194.899
2MASS J14392836+1929149	L1	242	$70.56 \pm 0.18$	0.0267	0.288	170.356
Kelu 1	L2	155	$49.05 \pm 0.73$	0.0373	0.597	31.687
2MASS J15065441+1321060	L3	148	$85.43 \pm 0.19$	0.0366	0.197	174.515
2MASS J00361617+1821104	L3.5	150	$114.47 \pm 0.14$	0.0181	0.110	299.883
2MASS J22244381-0158521	L4.5	305	$86.15 \pm 0.41$	0.0483	0.193	77.989
2MASS J15074769-1627386	L5	114	$134.95 \pm 0.26$	0.0236	0.079	170.433
VHS 1256-1257 B	L7	293	$45 \pm 2.4$	0.589	0.709	1.59
2MASS J08251968+2115521	L7.5	97	$92.60 \pm 0.82$	0.1290	0.167	12.888
DENIS-P J025503.3-470049	L8	65	$205.40 \pm 0.18$	0.0303	0.034	48.591
SDSS J125453.90-012247.4	T2	266	$74.18 \pm 2.31$	0.1829	0.261	4.812
2MASS J05591915-1404489	T5	1025	$95.27 \pm 0.72$	0.0803	0.158	32.561

<sup>a</sup> Spectral types are taken from M. C. Cushing et al. (2005) or J. T. Rayner et al. (2009). The spectral type of VHS 1256-1257 B is taken from B. Gauza et al. (2015).

<sup>b</sup> Parallax values are reported in milliarcseconds and are taken from *Gaia* data releases ( Gaia Collaboration et al. 2021). The parallax for VHS 1256-1257 B is taken from T. J. Dupuy et al. (2020)

<sup>c</sup> The best-fit scale factor from Equation 1

<sup>d</sup> The expected scale factor accounts for the different parallax measurements for HD 33632 and the template dwarfs. It assumes a good spectral match and similar object radii

<sup>e</sup> The difference between the fitted scale parameter and the expected scale parameter in units of the propagated uncertainty.

**Table 3.** Synthetic Atmosphere Model Grid Parameter Ranges

Parameter	Range
Sonora Elf Owl	
$T_{\text{eff}}$	1300 K – 2200 K, 100 K steps
$\log(g)$	3.25 - 5.5, 0.25 dex steps
$\log(K_{\text{zz}})$	2, 4, 7, 8, 9
$\log(\frac{z}{z_0})$	-1.0, -0.5, 0.0, 0.5, 0.7, 1.0
$C/O$	0.5 – 2.5, 0.5 steps
Sonora Diamondback	
$T_{\text{eff}}$	900 K – 2400 K, 100 K steps
$\log(g)$	3 – 5.5, 0.25 dex steps
$\log(\frac{z}{z_0})$	-0.5 – 0.5, 0.5 dex steps
$f_{\text{sed}}$	1, 2, 3, 4, 8, nc
Exo-REM	
$T_{\text{eff}}$	400 K – 2000 K, 50 K steps
$\log(g)$	3.00 - 5.0, 0.5 dex steps
$\log_{10}(\frac{z}{z_0})$	-0.5 – 2, 0.5 dex steps
$C/O$	0.1 – 0.8, 0.05 steps
Barman/Brock	
$T_{\text{eff}}$	800 K – 1600 K, 100 K steps
$\log(g)$	4.75, 5.0, 5.5
$P_c$	10 bar – 30 bar, 10 bar steps
$a_0$	0.25 $\mu\text{m}$ – 0.5 $\mu\text{m}$ , 0.25 $\mu\text{m}$ steps

in this case. For Elf Owl, analysis of an interpolated grid was too computationally expensive given the high-dimensionality of the models. This concern also applies to the Exo-REM models.

Best-fit models are determined by maximizing the logarithm of the posterior function,

$$\log \mathcal{P} = -0.5\chi^2 + \log(\mathcal{G}) + \log\left(\frac{1}{R}\right) \quad (2)$$

Where  $\chi^2$  is calculated as

$$\chi^2(\boldsymbol{\tau}, R, \varpi) = \left( ((R\varpi)^2 x(\boldsymbol{\tau}) - \boldsymbol{\mu})^T \boldsymbol{\Sigma}^{-1} (((R\varpi)^2 x(\boldsymbol{\tau}) - \boldsymbol{\mu})) \right), \quad (3)$$

similar to Equation 1 with  $\boldsymbol{\mu}$  the measured spectrum of HD 33632 Ab,  $\boldsymbol{\Sigma}$  the data covariance matrix, and  $x(\boldsymbol{\tau})$  the model spectrum with parameters  $\boldsymbol{\tau}$ , including effective temperature, surface gravity, and other model-specific composition and cloud structure variables. Here we replace the scale factor in Equation 1 with the square of the product of  $R$ , the

object radius, and  $\varpi$  the object parallax. The prior,  $\mathcal{G}$ , incorporates the *Gaia* parallax measurement and uncertainty  $37.8953 \pm 0.0262$  milliarcseconds ( *Gaia* Collaboration et al. 2021),

$$\mathcal{G}(\varpi) = \frac{1}{\sqrt{2\pi(0.0262)^2}} e^{-\frac{(\varpi-37.8953)^2}{2(0.0262)^2}}. \quad (4)$$

The last term in Equation 2 represents a log-uniform prior on the object radius. At this stage, we do not explicitly apply priors to model parameters, resulting in uniform priors for linear variables ( $T_{\text{eff}}$ ,  $C/O$ ) and log-uniform priors on logarithmic variables ( $\log(g)$ ,  $\log K_{\text{zz}}$ ,  $\log(\frac{z}{z_0})$ ).

We employ a brute-force, grid-fitting method testing each model in each grid using 266 steps in object radius from  $0.5 R_{\text{Jup}}$  to  $2.5 R_{\text{Jup}}$ , and 66 steps in parallax spanning 37.79 to 38.00 milliarcseconds (or  $\text{kpc}^{-1}$ ).

We show the best-fitting models from each grid with green markers in the panels of Figure 5. Formal parameter uncertainties for atmospheric parameters in each case are very tight, not extending beyond one grid point at the 95% confidence level for all grids except Exo-REM. For the Exo-REM grid, there is one additional model within 95% confidence. In all cases there is a small uncertainty in radius and parallax, but the precise *Gaia* parallax measurement is highly constraining.

## 4. DISCUSSION

### 4.1. Evaluating Fits of Synthetic Spectra

In Figure 5 it is clear that the cloudy grids can better approximate the SED of HD 33632 Ab. This is not surprising given the  $\sim L9$  spectral type suggested by our analysis in Section 3.2. The best-fit cloud parameters suggest vertically extended clouds with both  $f_{\text{sed}}$  and  $P_c$  at their grid limits for cloud thickness. These parameter values are somewhat at odds with expectations for an L9-type object, where the processes of cloud particle precipitation and dispersal that drive the L/T transition should have begun (D. C. Stephens et al. 2009; L. Brock et al. 2021).

Across the grids, best-fit effective temperatures range from 1250 K to 1500 K, best-fit surface gravities range from  $\log(g) = 3.25 - 5.0$ , and best fit metallicity ranges from  $\log(\frac{z}{z_0}) = -0.5 - 0.0$  suggesting systematic uncertainty much larger than the less-than-one-grid-step formal fit uncertainty within each grid.

### 4.2. Atmosphere Fits Compared to Evolutionary Models

We compare the best-fit atmospheric model parameters presented in the previous Section to the predictions of several brown dwarf evolution models. For this purpose, we assume the mass and age constraints are uncorrelated and create  $10^5$  (age, mass) pairs, drawing ages from a normal distribution with mean 1.7 Gyr and a standard deviation of 0.4 Gyr (based on the results of G. M. Brandt et al. 2021) and masses from

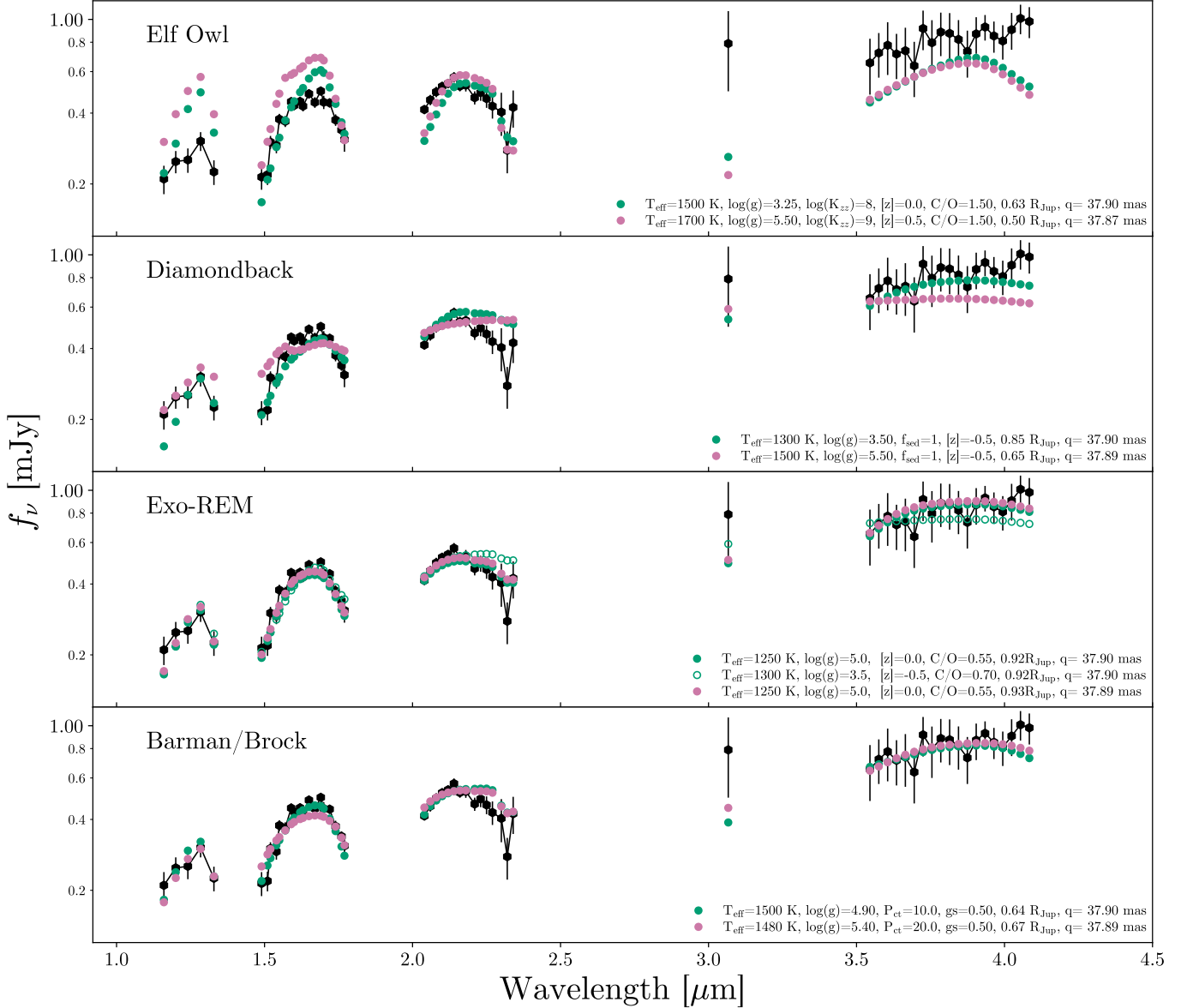


**Figure 5.** Best-fit synthetic atmosphere models from four model grids. In each case, green markers show fits with a gaussian prior on parallax, a log-flat prior on radius and surface gravity and a flat prior on effective temperature. Where applicable, a log-flat prior is used on metallicity and  $K_{zz}$  and flat priors on C/O, and cloud parameters. Pink markers use a joint prior on mass and surface gravity informed by dynamical mass constraints. See text for details.

a generalized extreme value distribution (A. Possolo et al. 2019) representing a mass constraint of  $52.8^{+2.6}_{-2.4} M_{\text{Jup}}$  (M. El Morsy et al. 2025). We then use SPLAT (A. J. Burgasser & Splat Development Team 2017) to interpolate a variety of evolution models at each of the age-mass pairs to produce distributions of effective temperature, surface gravity, and object radius.

For this work, we manually add the Sonora Diamondback evolution model data into SPLAT to take advantage of its interpolation architecture. Results for the Sonora Diamon-

back hybrid cloud models at different metallicities as well as the Diamondback cloud free models are shown in Figure 6. The A. Burrows et al. (2001) and I. Baraffe et al. (2015) models are also displayed. While there is some variation in the predictions of the various models, especially when considering cloudy versus no-cloud models, it is clear that it is very unlikely for HD 33632 Ab to have a surface gravity below  $\log(g) = 5.0$  or a radius below  $0.75 R_{\text{Jup}}$ . Only the higher-gravity Exo-REM model is consistent with these expectations. For the other grids, the best-fit atmospheres fall

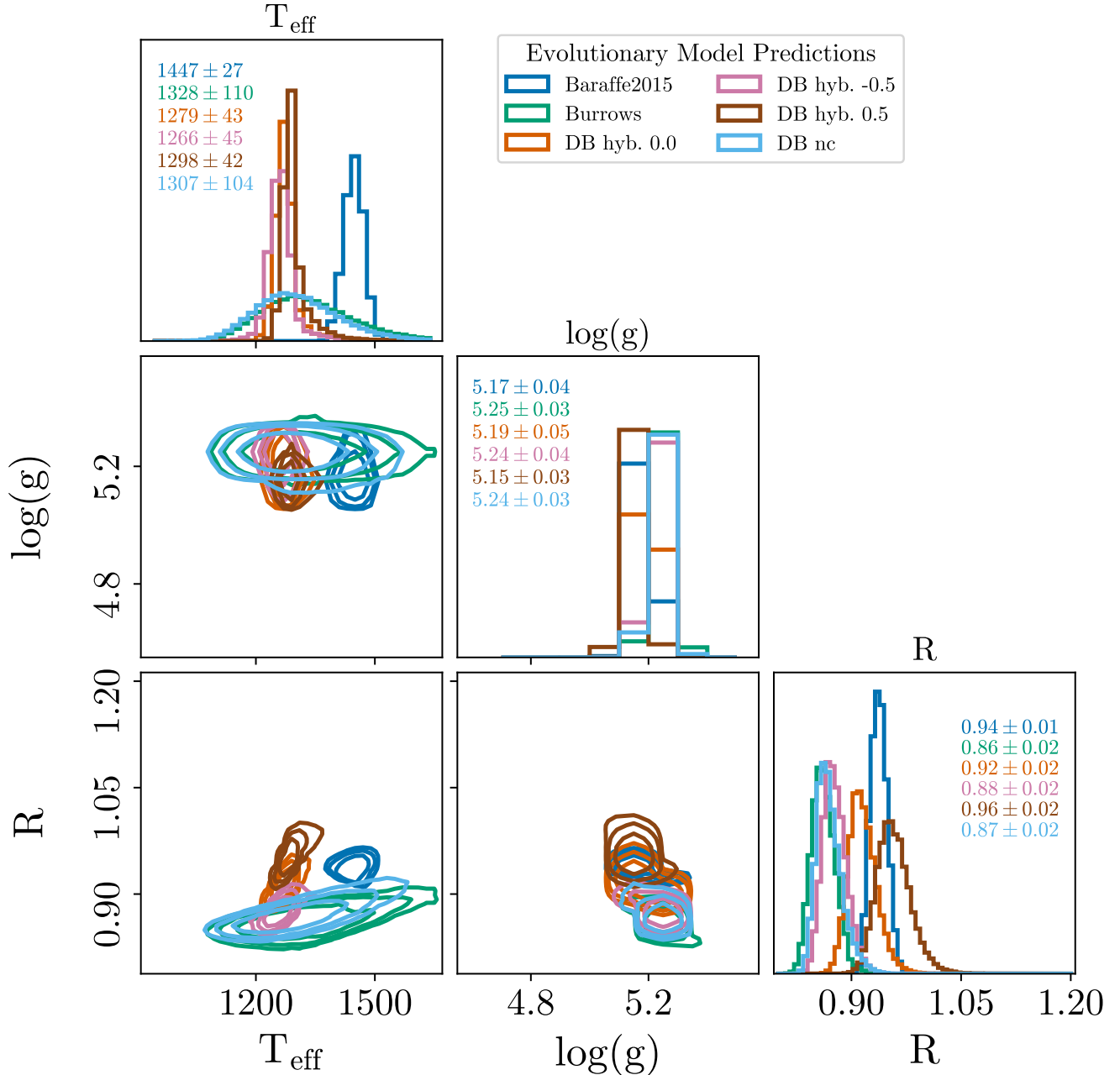


**Figure 6.** The distribution of evolutionary model predictions for HD 33632 Ab after propagating uncertainties in the system age and companion mass.

outside this range for at least one parameter. Consequently, a sense of unreliability surrounds the interpretation of the model parameters, especially those that are known to correlate with surface gravity, like metallicity (e.g., A. J. Skemer et al. 2016).

#### 4.2.1. Mass Constrained Fits

In search of more physically plausible atmosphere models, we re-run our fits to the data using a joint prior on object

radius and surface gravity based on the precise dynamical mass measurement. In this case, we optimize

$$\log \mathcal{P} = -0.5\chi^2 + \log(\mathcal{G}) + \log(\mathcal{O}), \quad (5)$$

where  $\chi^2$  and  $\mathcal{G}$  are as described above, and  $\mathcal{O}$  is

$$\mathcal{O} = \frac{1}{\sqrt{2\pi(2.5)^2}} e^{-\frac{(m-52.8 M_{\text{Jup}})^2}{2(2.5 M_{\text{Jup}})^2}}, \quad (6)$$

with  $m = \frac{gR^2}{G}$ ,  $g$  the surface gravity,  $R$  the object radius, and  $G$  the gravitational constant. These fits are shown in Figure 5, with pink markers.

This approach alleviates some tension with evolutionary model predictions for surface gravity in the Sonora models, but in each case tension with expectations for the object radius are increased. Since we did not interpolate these grids, the coarse sampling challenges the fitting algorithm as no option is well suited to satisfy the mass prior with a reasonable radius.

For the interpolated Barman/Brock models, this approach resulted in smaller changes to best-fit model parameters, partly because the best-fit previously had a surface gravity more in line with expectations compared to the Sonora models. The object radius did increase some, but not enough to coincide with the range of evolutionary model predictions. The  $P_c$  parameter increased, suggesting a deeper cloud and better tuned cloud structure may be necessary to fit the data.

The dynamical-mass based prior rules out the low-gravity, low-metallicity, high C/O Exo-REM model, leaving only the higher-gravity, solar composition model. This model is nearly a perfect match to the predictions of the evolutionary models, with the surface gravity,  $\log(g) = 5$ , being slightly too low. However, the Exo-REM grid does not include models above  $\log(g) = 5$ , so the small, 0.1 dex, discrepancy can be understood as a limitation of the grid range. We note that our optimal Exo-REM model is the same as that found by [M. El Morsy et al. \(2025\)](#) in their fits to Charis and NIRC2 data alone.

#### 4.2.2. Investigating Cloud Structure

Since our interpolated Barman/Brock models include the effective temperature and surface gravity predicted by evolutionary models, we run an additional constrained fit for this grid. We again make use of Equation 2 now using evolutionary model predictions to restrict  $T_{\text{eff}}$  to the range 1100-1600,  $\log(g)$  to the range 5.05 – 5.35, and Radius to the range 0.8 – 1.02  $R_{\text{Jup}}$ . The best-fit from this approach is shown in each row of Figure 7 with blue markers.

The constrained fit includes a deeper cloud with larger grains than the unconstrained fit, consistent with our understanding of the processes driving the L/T transition ([L. Brock et al. 2021](#)). Overall the model is reasonably close to the data, however it is too bright in the K-band and too flat in the L-band.

In Figure 7 we show how the model varies as a function of the four free parameters, to provide some guidance in interpreting the remaining tension between the model and the data. We let the overall flux scaling (that is, the object radius) vary for an optimal fit in each case to emphasize differences in spectral shape.

Effective temperature is constrained by the near-IR colors, specifically the J-band flux scaling relative to H and K-band. Colder models begin to exhibit stronger methane absorption at  $\sim 3.3 \mu\text{m}$ . Surface gravity changes of 0.3 dex in either direction do not seem to cause large changes in the model spectra, outside the unconstrained region between  $\sim 2.4 \mu\text{m} - 3.1 \mu\text{m}$ . The mean cloud particle size changes both the spectral slope across the L-band and the relative scaling of the J and H bands compared to K-band. The optimal fit prefers to match the near-IR data at the expense of a relatively poor fit to the ALES data, owing to the larger number of high signal-to-noise data points in the near-IR. However, the spectral slope of the ALES data suggests that a tuned model with smaller cloud particles may be necessary to provide a good fit. Varying the cloud top-pressure results in significant variation in the model spectra, especially at the wavelengths corresponding to the P-, Q-, and R-branch ro-vibrational transitions of methane,  $\sim 3.1 \mu\text{m} - 3.7 \mu\text{m}$ . Our inability to detect HD 33632 Ab between  $\sim 3.1 \mu\text{m} - 3.5 \mu\text{m}$ , may suggest low intrinsic flux through this range, possibly due to deeper cloud structures. Evidently, constraining the architecture of clouds in the atmosphere of HD 33632 Ab would greatly benefit from measurements in this range. ALES observations under better telluric throughput conditions than presented here could contribute meaningful constraints in this range.

#### 4.3. Comparison to HR 8799 c, d, e

HD 33632 Ab exhibits spectral similarity to the planets in the HR 8799 system, which also have spectral types at the L/T transition (e.g., [A. Z. Greenbaum et al. 2018](#)). In Figure 8, we compare the 1 – 4.1  $\mu\text{m}$  spectrum of HD 33632 Ab to the spectra of HR 8799 c, d, and e (including data from [D. S. Doelman et al. 2022](#); [R. Galicher et al. 2011](#); [A. J. Skemer et al. 2014](#); [A. Zurlo et al. 2016](#); [B. R. Oppenheimer et al. 2013](#); [A. Z. Greenbaum et al. 2018](#); [E. Nasedkin et al. 2024](#)). All spectra have been scaled to a distance of 10 pc to facilitate comparison.

Spectral analysis suggests that HD 33632 Ab has an effective temperature  $\sim 200 \text{ K}$  warmer than the three HR 8799 planets considered here ([D. S. Doelman et al. 2022](#)). Consequently, the close overlap in general flux level between the planets and HD 33632 Ab provides evidence that the younger planets have larger radii, consistent with our expectations from evolutionary models.

In the K-band, major opacity sources include collisionally induced absorption of molecular hydrogen, and ro-vibrational bands of both methane and carbon monoxide. Combined, these opacity sources result in K-band flux being highly-sensitive to photospheric pressure, which is effected by surface gravity, metallicity, and clouds. The lower K-band flux of HD 33632 Ab compared to the planets, must

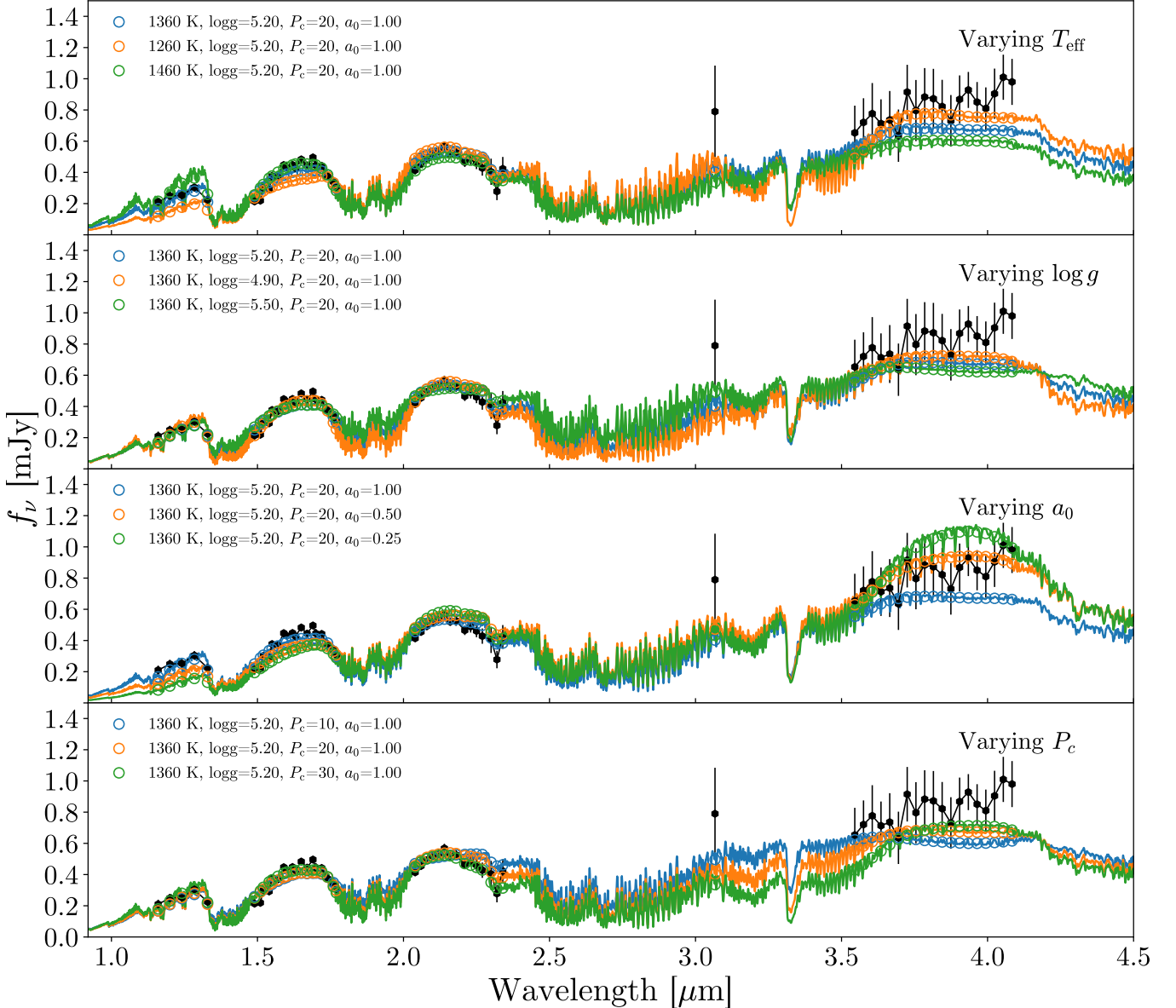


**Figure 7.** Varying atmosphere model parameters for HD 33632 Ab around the best evolutionary model-constrained fit from the Barman/Brock grid.

in part be due to significantly higher surface gravity in the more evolved (smaller radius) and more massive object.

HR 8799 d has a lower J-band flux and a flatter L-band spectral slope than HD 33632 Ab. Figure 7 shows that J-band flux relative to the other bands is affected by changes in temperature and cloud particle size. We also see that L-band spectral slope is affected by cloud particle size. HR 8799 d and HD 33632 Ab likely have different temperatures and cloud structures.

## 5. CONCLUSION

We present high-contrast ALES integral field spectroscopy observations of the HD 33632 system, resulting in a flux calibrated 3 – 4.12  $\mu\text{m}$  spectrum of the brown dwarf companion HD 33632 Ab. We compile a spectral energy distribution for the brown dwarf combining Subaru/Charis data with our new LBTI/ALES data. The low-resolution 1 – 4.12  $\mu\text{m}$  spectrum is matched to late L-dwarf template spectra with best fits found for field-age L7–L9 type objects (Figure 4).

Synthetic atmosphere models with clouds provide a reasonably close match to the data (Figure 5), however, the

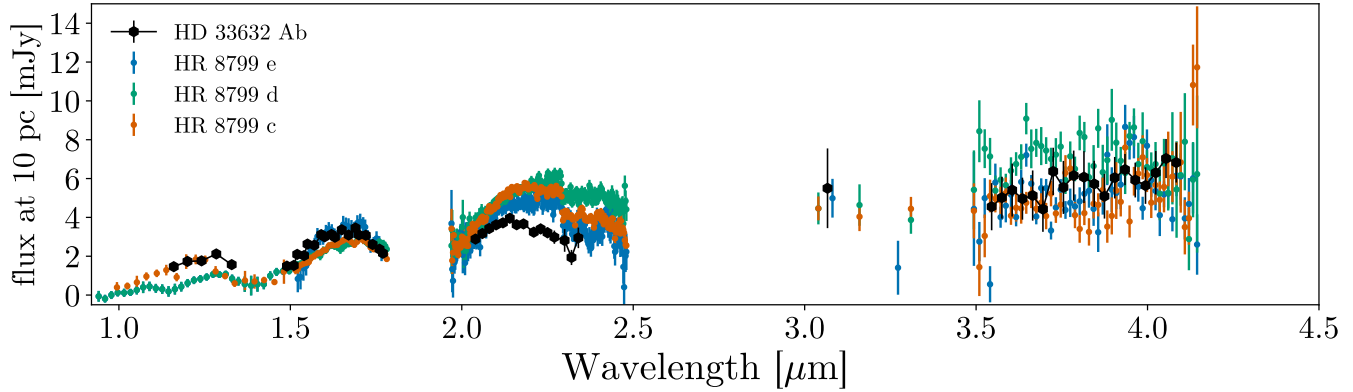


**Figure 8.** HD 33632 Ab compared to the SEDs of HR 8799 c, d, e adopted from D. S. Doelman et al. (2022) and using the K-band measurements from E. Nasedkin et al. (2024).

cloud-free Elf Owl models do not reproduce the shape of the SED. This is consistent with clouds playing a central role in shaping the appearance of L-dwarf spectra.

Dynamical constraints from radial velocity monitoring and astrometric measurements of the system yield a tight mass constraint on HD 33632 Ab (M. El Morsy et al. 2025). Combining mass with age estimates for the system enables the use of brown dwarf evolutionary models to predict the bulk physical properties of HD 33632 Ab. Various families of evolutionary models each including different treatment of clouds and different bulk metallicities all suggest a tight distribution of surface gravities and object radii when uncertainty in mass and age are propagated (Figure 6). Our best-fit model atmospheres imply significant tension with the evolutionary model consensus, suggesting unphysical best-fit parameters and creating some uncertainty in the interpretation of parameters like metallicity and C/O ratio.

We demonstrate an atmosphere model fitting approach using a joint prior on mass and gravity based on dynamical constraints. This approach emphasized the need for finely sampled grids when using such precise mass measurements. Application of mass-based priors to our interpolated grid of Barman/Brock models did alleviate some of the tension with evolutionary models, but the best fit radius is still  $\sim 30\%$  too

small. For the Exo-REM grid, the mass-based prior rules out fits incompatible with evolutionary model predictions.

We run a third optimization approach using the predictions of evolutionary models directly as priors in our atmosphere fit. Given the tight evolutionary model constraints we only apply this to the interpolated Barman/Brock models. This exercise identifies a deeper cloud with larger grains than the unconstrained fit, consistent with expectations for the L/T transition (L. Brock et al. 2021).

Finally, we compare to HR 8799 c, d, and e, showing general spectroscopic similarities between the L/T transition objects, but with significant differences likely due to differences in temperature, surface gravity, and cloud structure.

An on-going LBTI/ALES observational program and an independent JWST Cycle 4 NIRSpec IFU program both aim to collect thermal-IR spectroscopy for an emerging population of directly imaged companions whose association with a more massive host star facilitate dynamical mass constraints from *Gaia* and compositional constraints from stellar spectroscopic analysis. The goal of both of these efforts is to create a spectroscopic library of objects with constrained physical parameters to facilitate progress in understanding the complex physical processes sculpting the dramatic L/T transition and cloud processes in general.

## APPENDIX

### A. SIGNAL-TO-NOISE MAPS FOR SELECTED WAVELENGTH SLICES

In Figure 9, we show signal-to-noise (S/N) maps for selected wavelength slices and our median collapsed cube. For this purpose, the signal in each pixel is taken as the PSF-weighted mean flux in an aperture centered on that pixel with radius  $\lambda/D$ , and noise as the standard deviation of flux measurements in non-overlapping apertures at the same projected separation.

Detector crosstalk results in pixels aligned with the host star exhibiting complex structure in ALES cubes (D. S. Doelman et al. 2022). In our S/N maps, we mask the regions to the North and South most affected by crosstalk. An inset image in each panel of Figure 9 highlights the optimization region used in our negative-planet-injection approach to companion photometry.

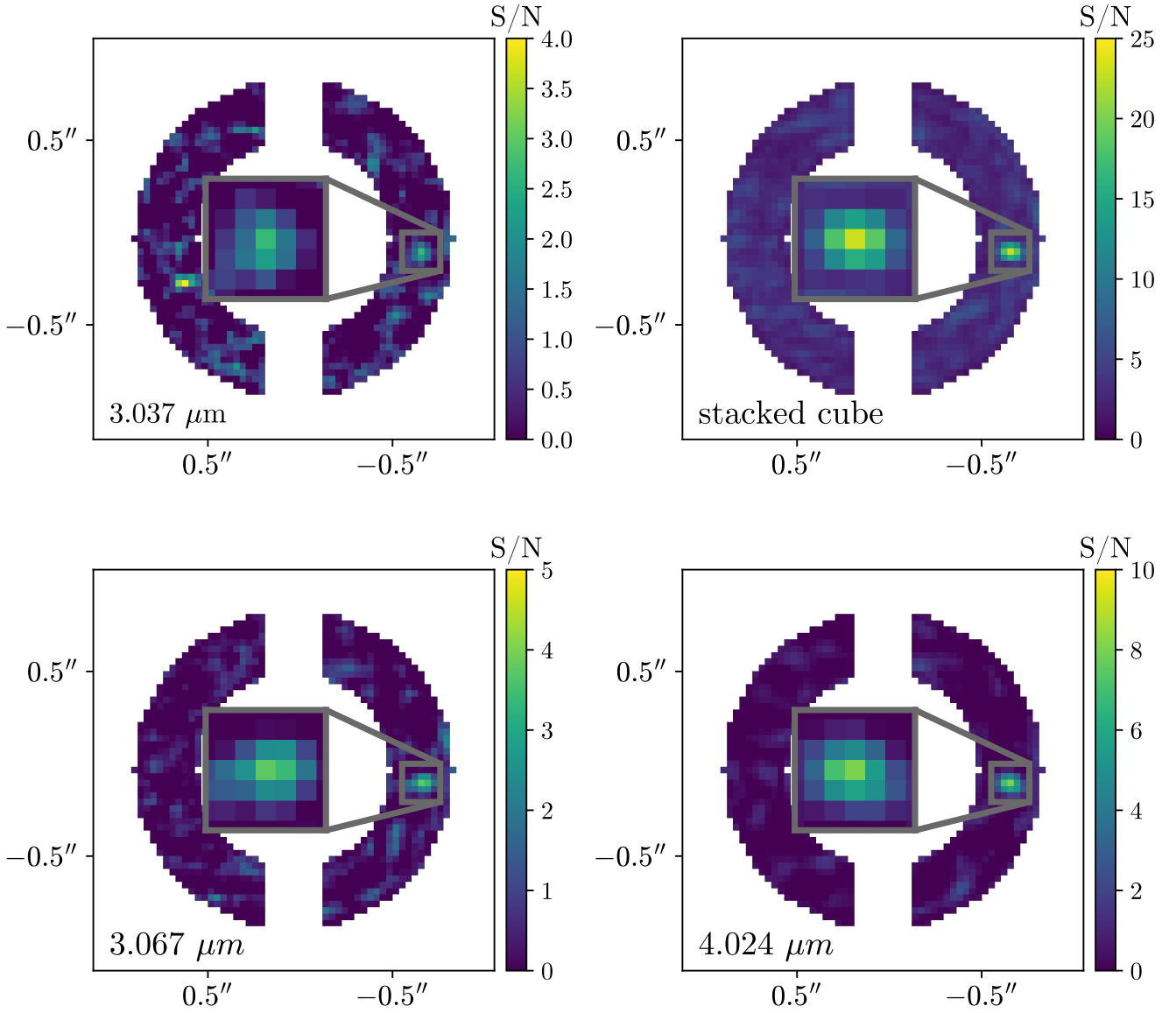


**Figure 9.** Signal-to-noise maps for three wavelength slices and the median combined spectral cube for our 2021-02-28 ALES observations of HD 33632 Ab. The inset for each panel highlights the optimization region used for extracting companion photometry using an iterative negative-planet injection strategy (see Section 2.4)

#### ACKNOWLEDGEMENTS

We thank the LBT director for allocating director’s discretionary time to this project. Thanks to Ilya Ilyin and Jennifer Power for their support collecting data for this program.

This work benefited from the Exoplanet Summer Program in the Other Worlds Laboratory (OWL) at the University of California, Santa Cruz, a program funded by the Heising-Simons Foundation.

Support for basic research at the U.S. Naval Research Laboratory comes from the 6.1 base program. This paper is based on work funded by NSF Grants 1608834, 1614320 and 1614492.

The LBT is an international collaboration among institutions in the United States, Italy and Germany. LBT Corporation partners are: The University of Arizona on behalf of the Arizona university system; Istituto Nazionale di Astrofisica, Italy; LBT Beteiligungsgesellschaft, Germany, representing the Max-Planck Society, the Astrophysical Institute Potsdam, and Heidelberg University; The Ohio State University, and The Research Corporation, on behalf of The University of Notre Dame, University of Minnesota, and University of Virginia. We thank all LBTI team members for their efforts that enabled this work.

*Facilities:* LBT (LBTI/LMIRCam, LBTI/ALES)

*Software:* Astropy (Astropy Collaboration et al. 2013), Matplotlib (J. D. Hunter 2007), Scipy (P. Virtanen et al. 2020), SPLAT (A. J. Burgasser & Splat Development Team 2017),

## REFERENCES

- Amara, A., & Quanz, S. P. 2012, MNRAS, 427, 948, doi: [10.1111/j.1365-2966.2012.21918.x](https://doi.org/10.1111/j.1365-2966.2012.21918.x)
- Astropy Collaboration, Robitaille, T. P., Tollerud, E. J., et al. 2013, A&A, 558, A33, doi: [10.1051/0004-6361/201322068](https://doi.org/10.1051/0004-6361/201322068)
- Baraffe, I., Homeier, D., Allard, F., & Chabrier, G. 2015, A&A, 577, A42, doi: [10.1051/0004-6361/201425481](https://doi.org/10.1051/0004-6361/201425481)
- Barman, T. S., Konopacky, Q. M., Macintosh, B., & Marois, C. 2015, ApJ, 804, 61, doi: [10.1088/0004-637X/804/1/61](https://doi.org/10.1088/0004-637X/804/1/61)
- Barman, T. S., Macintosh, B., Konopacky, Q. M., & Marois, C. 2011, ApJL, 735, L39, doi: [10.1088/2041-8205/735/2/L39](https://doi.org/10.1088/2041-8205/735/2/L39)
- Baudino, J. L., Bézard, B., Boccaletti, A., et al. 2015, A&A, 582, A83, doi: [10.1051/0004-6361/201526332](https://doi.org/10.1051/0004-6361/201526332)
- Blain, D., Charnay, B., & Bézard, B. 2021, A&A, 646, A15, doi: [10.1051/0004-6361/202039072](https://doi.org/10.1051/0004-6361/202039072)
- Bonavita, M., Fontanive, C., Gratton, R., et al. 2022, MNRAS, 513, 5588, doi: [10.1093/mnras/stac1250](https://doi.org/10.1093/mnras/stac1250)
- Brandt, G. M., Brandt, T. D., Dupuy, T. J., Michalik, D., & Marleau, G.-D. 2021, ApJL, 915, L16, doi: [10.3847/2041-8213/ac0540](https://doi.org/10.3847/2041-8213/ac0540)
- Brandt, T. D., Rizzo, M., Groff, T., et al. 2017, Journal of Astronomical Telescopes, Instruments, and Systems, 3, 048002, doi: [10.1117/1.JATIS.3.4.048002](https://doi.org/10.1117/1.JATIS.3.4.048002)
- Brock, L., Barman, T., Konopacky, Q. M., & Stone, J. M. 2021, ApJ, 914, 124, doi: [10.3847/1538-4357/abfc46](https://doi.org/10.3847/1538-4357/abfc46)
- Burgasser, A. J., Geballe, T. R., Leggett, S. K., Kirkpatrick, J. D., & Golimowski, D. A. 2006, ApJ, 637, 1067, doi: [10.1086/498563](https://doi.org/10.1086/498563)
- Burgasser, A. J., & Splat Development Team. 2017, in Astronomical Society of India Conference Series, Vol. 14, Astronomical Society of India Conference Series, 7–12. <https://arxiv.org/abs/1707.00062>
- Burrows, A., Hubbard, W. B., Lunine, J. I., & Liebert, J. 2001, Reviews of Modern Physics, 73, 719, doi: [10.1103/RevModPhys.73.719](https://doi.org/10.1103/RevModPhys.73.719)
- Calamari, E., Faherty, J. K., Visscher, C., et al. 2024, ApJ, 963, 67, doi: [10.3847/1538-4357/ad1f6d](https://doi.org/10.3847/1538-4357/ad1f6d)
- Carnall, A. 2021, SpectRes: Simple spectral resampling,, Astrophysics Source Code Library, record ascl:2104.019 <http://ascl.net/2104.019>
- Charnay, B., Bézard, B., Baudino, J. L., et al. 2018, ApJ, 854, 172, doi: [10.3847/1538-4357/aaac7d](https://doi.org/10.3847/1538-4357/aaac7d)
- Currie, T., Brandt, T. D., Kuzuhara, M., et al. 2020, ApJL, 904, L25, doi: [10.3847/2041-8213/abc631](https://doi.org/10.3847/2041-8213/abc631)
- Currie, T., Brandt, G. M., Brandt, T. D., et al. 2023, Science, 380, 198, doi: [10.1126/science.abo6192](https://doi.org/10.1126/science.abo6192)
- Cushing, M. C., Rayner, J. T., & Vacca, W. D. 2005, ApJ, 623, 1115, doi: [10.1086/428040](https://doi.org/10.1086/428040)
- Cutri, R. M., & et al. 2012, VizieR Online Data Catalog, II/311
- Doelman, D. S., Stone, J. M., Briesemeister, Z. W., et al. 2022, AJ, 163, 217, doi: [10.3847/1538-3881/ac5d52](https://doi.org/10.3847/1538-3881/ac5d52)
- Dupuy, T. J., Liu, M. C., Magnier, E. A., et al. 2020, Research Notes of the American Astronomical Society, 4, 54, doi: [10.3847/2515-5172/ab8942](https://doi.org/10.3847/2515-5172/ab8942)
- El Morsy, M., Currie, T., Bovie, D., et al. 2025, ApJ, 981, 20, doi: [10.3847/1538-4357/ada3be](https://doi.org/10.3847/1538-4357/ada3be)
- Ertel, S., Hinz, P. M., Stone, J. M., et al. 2020, in Society of Photo-Optical Instrumentation Engineers (SPIE) Conference Series, Vol. 11446, Optical and Infrared Interferometry and Imaging VII, ed. P. G. Tuthill, A. Mérand, & S. Sallum, 1144607, doi: [10.1117/12.2561849](https://doi.org/10.1117/12.2561849)
- Gaia Collaboration, Prusti, T., de Bruijne, J. H. J., et al. 2016, A&A, 595, A1, doi: [10.1051/0004-6361/201629272](https://doi.org/10.1051/0004-6361/201629272)
- Gaia Collaboration, Brown, A. G. A., Vallenari, A., et al. 2021, A&A, 649, A1, doi: [10.1051/0004-6361/202039657](https://doi.org/10.1051/0004-6361/202039657)
- Galicher, R., Marois, C., Macintosh, B., Barman, T., & Konopacky, Q. 2011, ApJL, 739, L41, doi: [10.1088/2041-8205/739/2/L41](https://doi.org/10.1088/2041-8205/739/2/L41)
- Gauza, B., Béjar, V. J. S., Pérez-Garrido, A., et al. 2015, The Astrophysical Journal, 804, 96, doi: [10.1088/0004-637X/804/2/96](https://doi.org/10.1088/0004-637X/804/2/96)
- Gibbs, A. B., Lewis, B. L., Fitzgerald, M. P., et al. 2024, ApJ, 973, 119, doi: [10.3847/1538-4357/ad64cc](https://doi.org/10.3847/1538-4357/ad64cc)

- Gray, R. O., Corbally, C. J., Garrison, R. F., McFadden, M. T., & Robinson, P. E. 2003, *AJ*, 126, 2048, doi: [10.1086/378365](https://doi.org/10.1086/378365)
- Greco, J. P., & Brandt, T. D. 2016, *ApJ*, 833, 134, doi: [10.3847/1538-4357/833/2/134](https://doi.org/10.3847/1538-4357/833/2/134)
- Greenbaum, A. Z., Pueyo, L., Ruffio, J.-B., et al. 2018, *AJ*, 155, 226, doi: [10.3847/1538-3881/aabc8](https://doi.org/10.3847/1538-3881/aabc8)
- Hinz, P. M., Defrère, D., Skemer, A., et al. 2016, in Society of Photo-Optical Instrumentation Engineers (SPIE) Conference Series, Vol. 9907, Optical and Infrared Interferometry and Imaging V, ed. F. Malbet, M. J. Creech-Eakman, & P. G. Tuthill, 990704, doi: [10.1117/12.2233795](https://doi.org/10.1117/12.2233795)
- Horne, K. 1986, *PASP*, 98, 609, doi: [10.1086/131801](https://doi.org/10.1086/131801)
- Hsu, C.-C., Wang, J. J., Xuan, J. W., et al. 2024, *ApJ*, 971, 9, doi: [10.3847/1538-4357/ad58d3](https://doi.org/10.3847/1538-4357/ad58d3)
- Hunter, J. D. 2007, *Computing in Science Engineering*, 9, 90
- Leisenring, J. M., Skrutskie, M. F., Hinz, P. M., et al. 2012, in Society of Photo-Optical Instrumentation Engineers (SPIE) Conference Series, Vol. 8446, Ground-based and Airborne Instrumentation for Astronomy IV, 84464F, doi: [10.1117/12.924814](https://doi.org/10.1117/12.924814)
- Marois, C., Lafrenière, D., Doyon, R., Macintosh, B., & Nadeau, D. 2006, *ApJ*, 641, 556, doi: [10.1086/500401](https://doi.org/10.1086/500401)
- Mesa, D., Gratton, R., Kervella, P., et al. 2023, *A&A*, 672, A93, doi: [10.1051/0004-6361/202345865](https://doi.org/10.1051/0004-6361/202345865)
- Miles, B. E., & et al. 2023, *ApJL*, 946, L6, doi: [10.3847/2041-8213/acb04a](https://doi.org/10.3847/2041-8213/acb04a)
- Morley, C. V., Mukherjee, S., Marley, M. S., et al. 2024, *ApJ*, 975
- Mukherjee, S., Fortney, J. J., Morley, C. V., et al. 2024, *ApJ*, 963, 73, doi: [10.3847/1538-4357/ad18c2](https://doi.org/10.3847/1538-4357/ad18c2)
- Nasedkin, E., Mollière, P., Lacour, S., et al. 2024, *A&A*, 687, A298, doi: [10.1051/0004-6361/202449328](https://doi.org/10.1051/0004-6361/202449328)
- Oppenheimer, B. R., Baranec, C., Beichman, C., et al. 2013, *ApJ*, 768, 24, doi: [10.1088/0004-637X/768/1/24](https://doi.org/10.1088/0004-637X/768/1/24)
- Possolo, A., Merkatas, C., & Bodnar, O. 2019, *Metrologia*, 56, 045009, doi: [10.1088/1681-7575/ab2a8d](https://doi.org/10.1088/1681-7575/ab2a8d)
- Press, W. H., & Teukolsky, S. A. 1990, *Computer in Physics*, 4, 669, doi: [10.1063/1.4822961](https://doi.org/10.1063/1.4822961)
- Rayner, J. T., Cushing, M. C., & Vacca, W. D. 2009, *ApJS*, 185, 289, doi: [10.1088/0067-0049/185/2/289](https://doi.org/10.1088/0067-0049/185/2/289)
- Rice, M., & Brewer, J. M. 2020, *ApJ*, 898, 119, doi: [10.3847/1538-4357/ab9f96](https://doi.org/10.3847/1538-4357/ab9f96)
- Skemer, A. J., Hinz, P., Stone, J., et al. 2018, in Society of Photo-Optical Instrumentation Engineers (SPIE) Conference Series, Vol. 10702, Ground-based and Airborne Instrumentation for Astronomy VII, ed. C. J. Evans, L. Simard, & H. Takami, 107020C, doi: [10.1117/12.2314091](https://doi.org/10.1117/12.2314091)
- Skemer, A. J., Marley, M. S., Hinz, P. M., et al. 2014, *ApJ*, 792, 17, doi: [10.1088/0004-637X/792/1/17](https://doi.org/10.1088/0004-637X/792/1/17)
- Skemer, A. J., Morley, C. V., Zimmerman, N. T., et al. 2016, *ApJ*, 817, 166, doi: [10.3847/0004-637X/817/2/166](https://doi.org/10.3847/0004-637X/817/2/166)
- Sorahana, S., & Yamamura, I. 2014, *ApJ*, 793, 47, doi: [10.1088/0004-637X/793/1/47](https://doi.org/10.1088/0004-637X/793/1/47)
- Soummer, R., Pueyo, L., & Larkin, J. 2012, *ApJL*, 755, L28, doi: [10.1088/2041-8205/755/2/L28](https://doi.org/10.1088/2041-8205/755/2/L28)
- Stephens, D. C., Leggett, S. K., Cushing, M. C., et al. 2009, *ApJ*, 702, 154, doi: [10.1088/0004-637X/702/1/154](https://doi.org/10.1088/0004-637X/702/1/154)
- Stone, J. M., Skemer, A. J., Hinz, P., et al. 2018, in Society of Photo-Optical Instrumentation Engineers (SPIE) Conference Series, Vol. 10702, Ground-based and Airborne Instrumentation for Astronomy VII, ed. C. J. Evans, L. Simard, & H. Takami, 107023F, doi: [10.1117/12.2313977](https://doi.org/10.1117/12.2313977)
- Stone, J. M., Barman, T., Skemer, A. J., et al. 2020, *AJ*, 160, 262, doi: [10.3847/1538-3881/abbe3](https://doi.org/10.3847/1538-3881/abbe3)
- Stone, J. M., Skemer, A., Hinz, P., et al. 2022, in Society of Photo-Optical Instrumentation Engineers (SPIE) Conference Series, Vol. 12184, Ground-based and Airborne Instrumentation for Astronomy IX, ed. C. J. Evans, J. J. Bryant, & K. Motohara, 1218442, doi: [10.1117/12.2630308](https://doi.org/10.1117/12.2630308)
- Strassmeier, K. G., Ilyin, I., Järvinen, A., et al. 2015, *Astronomische Nachrichten*, 336, 324, doi: [10.1002/asna.201512172](https://doi.org/10.1002/asna.201512172)
- Tobin, T. L., Currie, T., Li, Y., et al. 2024, *AJ*, 167, 205, doi: [10.3847/1538-3881/ad3077](https://doi.org/10.3847/1538-3881/ad3077)
- Virtanen, P., Gommers, R., Oliphant, T. E., et al. 2020, *Nature Methods*, doi: <https://doi.org/10.1038/s41592-019-0686-2>
- Zhang, Z., Mollière, P., Hawkins, K., et al. 2023, *AJ*, 166, 198, doi: [10.3847/1538-3881/acf768](https://doi.org/10.3847/1538-3881/acf768)
- Zurlo, A., Vigan, A., Galicher, R., et al. 2016, *A&A*, 587, A57, doi: [10.1051/0004-6361/201526835](https://doi.org/10.1051/0004-6361/201526835)